Title: Context-Adaptive Nanotopology in Peptide Crystals

Authors: Vignesh Athiyarath[1], Elma Naranjo[1,2], Dhwanit Dave[1,7], Osman Goni Ridwan[3], Danilo A. Arturo Rodriguez[4], Qiang Zhu[3], Marta Monti[5], Gonzalo Díaz Mirón[5], Debarshi Banerjee[5,6], Ali Hassanali[6], Michelle C. Neary[7], Sheng Zhang[1], Rein V. Ulijn[1,7,8,9]*, Xi Chen[1,2,8,10]*

Affiliations:

[1]Advanced Science Research Center (ASRC) at the Graduate Center of the City University of New York, 85 St Nicholas Terrace, New York, 10031, USA.

[2]Department of Chemical Engineering, The City College of New York, 160 Convent Ave, New York, 10031, USA.

[3]Department of Mechanical Engineering and Energy Science, University of North Carolina at Charlotte (UNCC), Charlotte, 28223, USA.

[4]Department of Physics and Astronomy, University of Nevada Las Vegas, Las Vegas, 89154, USA.

[5]Condensed Matter and Statistical Physics, The Abdus Salam International Centre for Theoretical Physics, Trieste, 34151, Italy

[6]Scuola Internazionale Superiore di Studi Avanzati (SISSA), Trieste, 34136, Italy

[7]Department of Chemistry, Hunter College, City University of New York, New York, 10065, USA.

[8]Ph.D. Program in Chemistry, The Graduate Center of the City University of New York, New York, 10016, USA.

[9]Ph.D. Program in Biochemistry, The Graduate Center of the City University of New York, New York, 10016, USA.

[10]Ph.D. Program in Physics, The Graduate Center of the City University of New York, New York, 10016, USA.

*Corresponding authors. Emails: rulijn@gc.cuny.edu; xchen@gc.cuny.edu

Abstract: Biological systems, including proteins, employ water-mediated supramolecular interactions to adopt specific conformations for their functions. However, current solid-state supramolecular materials are typically stiff and fail to capture the dynamic behaviors observed in proteins. Here, we present dynamic crystal-hydrates of aliphatic dipeptides with sequence-isomers of leucine (L) and isoleucine (I). These crystals exhibit shallow conformational energy landscapes, with various reconfigurable crystal nano-architectures accessible through small changes in relative humidity and temperature. Specifically, for LI crystals, as water content changes, the solid-state supramolecular architecture rapidly and reversibly transitions between perpendicular and parallel honeycomb nano-architectures, as well as layered van der Waals structures, leading to significant and distinct variations in mechanical and photophysical properties. Our findings demonstrate the potential of leveraging aliphatic hydrophobic domains inspired by protein architectures to create dynamic solid-state materials with context-adaptive properties.

Main Text:

Biology's core concept of sequence-encoded assembly of functional structures through non-covalent interactions can be simplified and repurposed to create designed supramolecular materials[1–4]. Over the past few decades, this field of research has yielded a variety of supramolecular architectures[5] with remarkable mechanical[6], optical[7], and electronic properties[8]. Supramolecular assemblies are typically designed based on directional aromatic, electrostatic, and H-bonding patterns, resulting in stable and often stiff materials[9]. For instance, peptide materials can self-assemble into rigid architectures that are stabilized by aromatic zipper motifs and arrays of strong backbone-backbone H-bonding facilitated by water desolvation[10–13]. Recently, it has been demonstrated that the introduction of variable aliphatic tetrapeptide modules in supramolecular fibers dramatically regulates their dynamic features[14,15]. Metallo-dipeptide frameworks have been shown to have dynamically addressable pores for solvent inclusion[16]. These examples provide steps toward capturing the dynamic nature of proteins (Fig. 1a), which are agile and can undergo rapid conformation changes through hierarchical (re-) organization driven by non-covalent interactions among backbones, side chains, and solvents[17,18].

Proteins offer many examples that demonstrate how aliphatic amino acids, in particular leucine (**L**) and isoleucine (**I**), can be utilized to influence structures that are stable yet dynamic[19–24]. Besides preferential partitioning to exclude water, the side chains of these amino acids are abundant in -CH_2- rotors, affecting the steric packing and the strength of the stabilizing dispersion forces[25] that are reconfigurable[26] due to lower enthalpic gain and the plurality of rotationally allowed stabilizing configurations[20,21]. Aliphatic domains are consequently more adaptable than the directional and spatially restrictive interactions of aromatic residues, which occur through face-face, edge-face, or T-shaped interactions (Supplementary Fig. S1)[27]. Despite this versatility and their frequent involvement in dynamic reconfigurations in proteins, supramolecular materials incorporating arrays of aliphatic amino acids primarily exploit their hydrophobic effects, leading to relatively stable structures[14,28], *e.g.,* in designed **L**/**I** zippers[29,30]. The versatility of **L** and **I** inspired us to explore minimalistic aliphatic peptide assemblies to develop shallow-energy landscape materials that are reconfigurable in the solid-state through low-energy input, *e.g.,* by modulating the water activity using changes in external relative humidity (RH) and temperature control.

Here, we report dramatic and reversible conformer and topology interconversions of dipeptide crystalline hydrates in the solid state, which is enabled by the intricate interplay of the high degree of freedom in aliphatic side chain interactions of **L** and **I** combined with the H-bonding of water molecules within the lattice (Fig. 1b,c). Triggered by the partial displacement of water molecules through environmental RH and temperature variations, these transitions led to switching between a perpendicular nanoscale columnar architecture and a parallel honeycomb-like structure, as well as transitioning from either of these stiff structures to a soft lamellar van der Waals architecture, all underpinned by conformational changes in molecules that occur in the solid state (Fig. 1c). The readily interconverted hydrates exhibit distinct dynamic supramolecular properties, including significantly variable and addressable mechanical and photophysical properties governed by the intermolecular interactions between peptides and water.

Sequence-dependent dynamics of L and I dipeptides

Short peptides can serve as simple models for proteins[31], and decades of progress have demonstrated that they can be versatile building blocks for materials in their own right, providing access to properties that extend beyond biological systems[9,32]. To develop materials that readily reconfigure, we selected dipeptides **LL**, **II**, **IL**, and **LI**, which have previously been shown to form porous and layered crystal structures[33]. To explore their molecular dynamics, we first measured the solubilities of **LI**, **IL**, **II**, and **LL** dipeptides in water (Fig. 2a) and observed that these dipeptides exhibit drastically different, sequence-dependent solubilities of 0.66 mol L^{-1} (**II**), 0.57 mol L^{-1} (**IL**), 0.46 mol L^{-1} (**LI**), 0.1 mol L^{-1} (**LL**), which are up to two orders of magnitude higher than that of **FF** (0.008 mol L^{-1})[34], despite similar hydrophobicity. This observation illustrates that peptide solubility is not simply a reflection of hydropathy; rather, side chain flexibility and dispersion forces, influenced by sequence-imposed restrictions, contribute. The aqueous solubility of these aliphatic dipeptides is likely related to the formation of supramolecular dispersions—highly dynamic, soluble aggregates that do not precipitate and that are stabilized by weak hydrophobic forces enabled through assembly-induced conformer selection.

We next considered the relationship of conformer selection and assembly in the aqueous dispersions and the potential of these dipeptides to form dynamic structures in the solid state. To quantitatively relate the observed aggregation behaviors to solvent and peptide H-bonding and conformations, we first obtained their aggregation propensity (AP), which is quantified as the reduction in solvent-accessible surface area during assembly[35], and then examined H-bonding interactions and side chain dynamics and of these four dipeptides using molecular dynamic (MD) simulations. As expected, dipeptides with higher solubilities displayed lower AP scores: **II** (2.3) < **IL** (2.6) < **LI** (3.2) < **LL** (3.3) (Fig. 2a and Supplementary Fig. S2). The solubility also correlated well with a higher number of peptide-water H-bonds, a reduced number of peptide-peptide H-bonds (Fig. 2b), as well as the accessible surface areas of these dipeptides, which quantify side chain packing efficiency (Fig. 2c and Supplementary Note S1). We noted that the variation in AP and H-bonds correlated with the side chain dynamics of the dipeptides. For instance, while single dipeptides tend to have their side chains oriented on opposite sides of the backbone (θ ~120°), upon aggregation, they partially adapt to having both side chains on the same side (θ ~ 40°), favoring the segregation of hydrophilic and hydrophobic regions to form bilayer-like structures (Fig. 2d,e and Supplementary Fig. S3). The angles χ_1 and χ_2 of both **L** and **I** side chains also exhibited significant heterogeneity, with **L** showing higher variability than **I**. While the **I** side chains do not show significant sequence-dependent conformations, the χ_1 of **L** residue at the N-terminal and χ_2 of the **L** residue at the C-terminal are highly sequence-dependent (Fig. 2f,g, Supplementary Note S2 and Supplementary Fig. S4). In contrast, in **FF**, the π-stacked and conformationally restricted aromatic side chains are embedded inside the assembly, which reduces their exposure to water, resulting in lower solubility (AP = 3.49) (Supplementary Figs. S5,S6)[34,36]. Overall, the MD simulations suggested that the observed high dispersibility of **LI**, **IL**, **II**, and **LL** compared to **FF** is strongly correlated with the flexibility and dynamics of the aliphatic side chains facilitated by non-directional van der Waals interactions. The flexibility of the aliphatic side chain could lower the energy barriers for their dipeptide assembly to undergo configurational transitions. Along with previous observations, notably those by Görbitz, aliphatic dipeptides have solid-state structures with varying hydrophobic and hydrophilic domain packing arrangements through conformer selection[33], and we consequently anticipated a broad spectrum of dynamics, resulting in structures when water is removed or reintroduced that may be retained in the solid state.

Dynamic nature of hydrated L and I dipeptide crystalline hydrates

Upon evaporation of saturated aqueous dispersions, all these four dipeptides readily formed crystal hydrates with different structures and different degrees of water inclusion (Fig. 3a,b, Supplementary Note S3 and Supplementary Figs. S7-S9). The crystal structures characterized by single-crystal X-ray diffraction agree with those reported previously:

7LL•6H_2O (**$LL_{7:6}$**), 11IL•10H_2O (**$IL_{11:10}$**), II•2H_2O (**$II_{1:2}$**), and 2LI•5H_2O (**$LI_{2:5}$**)[33,37]. It is evident that **LL** and **IL** retain the low dihedral conformation of the solution dispersed state, forming stable needle-shaped crystals with aqueous nanopores separated by bilayers (similar to **FF**[38], while **II** and **LI** undergo a significant reorganization upon crystallization (Fig. 3b). Differences in packing lead to variations in surface hydrophobicity and porosity among these crystals, which, in turn, result in varying levels of water adsorption, as assessed by Dynamic Vapor Sorption (DVS). As RH increased from 5% to 95%, **$LL_{7:6}$**, **$LI_{2:5}$**, **$IL_{11:10}$**, and **$II_{1:2}$** adsorbed water corresponding to 36%, 18%, 0.89%, and 0.58% w/w, respectively (Supplementary Fig. S10).

Despite their different structures, all crystals are relatively stiff, exhibiting increasing Young's moduli of 13.2 GPa, 15.5 GPa, 16.1 GPa, and 27.2 GPa for **$LL_{7:6}$**, **$IL_{11:10}$**, **$II_{1:2}$**, and **$LI_{2:5}$**, with an increased relative amount of water content, as measured by atomic force microscopy (AFM) nanoindentation (Fig. 3c, Supplementary Note S4 and Supplementary Fig. S11). This observation was further validated by density-functional based tight-binding (DFTB) simulations[39] (Fig. 3d and Supplementary Figs. S12–S18). Notably, these aliphatic dipeptides exhibited a similar high stiffness to that of **FF** crystals (19-27 GPa), which are strengthened by the aromatic zipper topology[10].

Given the significant influence of water on the rigidity of these dipeptide crystals, we explored their phase changes through water removal at elevated temperatures using differential scanning calorimetry (DSC) and thermal gravimetric analysis (TGA) (Fig. 3e and Supplementary Note S5). Notably, the dipeptide crystal **$LI_{2:5}$** exhibited endothermic peaks at four distinct stages, occurring at widely separated temperatures of 74 °C, 106 °C, 133 °C, and 176 °C. The occurrence of multiple endothermic behaviors associated with water loss at lower temperatures suggests the potential existence of multiple equilibrium phases of the **$LI_{2:5}$** crystal that are close in energy and likely accessible by varying external stimuli of the chemical potential of water.

II$_{1:2}$ exhibited the next lowest endothermic peak, with a lack of weight loss, suggesting a reconfiguration that may not involve significant water loss. The **LL$_{7:6}$** and **IL$_{11:10}$** crystals showed similar peaks at relatively higher temperatures, indicating the stability of their channel configuration, a stable topology that resembles that of **FF**. Hence, **LI** and **II** were considered further as potential solid-state adaptive crystals.

Interconvertible crystal topologies accessed through changes in RH and temperature

Upon varying RH and temperature, we found that **LI$_{2:5}$** can reversibly undergo phase transitions among three distinct stable crystal structures with different water content (Fig. 4a and Supplementary Note S6), as observed by powder X-ray diffraction (PXRD) (Supplementary Fig. S19). When exposed to 55 °C/ 50% RH, **LI$_{2:5}$** crystals undergo a phase transition (Supplementary Fig. S19a) accompanied by water loss (6LI•5H_2O, **LI$_{6:5}$**), which was further validated by single-crystal XRD (Supplementary Table S1). Notably, the initial structure **LI$_{2:5}$** possessed a 3D honeycomb-like structure, where the **L**/**I** side chains formed a nanoscale hydrophobic column with a hydrophilic water-filled channel arranged perpendicular to it. The solid-state phase transition to **LI$_{6:5}$** resulted in a conversion of this columnar structure to a van der Waals layered structure, where the side chains of peptides form hydrophobic layers that stack along the z-axis (Fig. 4a and Supplementary Fig. S20a-c).

Interestingly, when heated to 60 °C at 50% RH, the **LI$_{2:5}$** crystals transformed upon further water loss to 4LI•3H_2O (**LI$_{4:3}$**)[37] (Fig. 4a and Supplementary Fig. S19b). This phase transition involved the change to another honeycomb-like structure, in which both the hydrophilic water and hydrophobic nanochannels are aligned parallel to each other (Fig. 4a and Supplementary Figs. S20d-f). **LI$_{4:3}$** can also spontaneously convert to **LI$_{6:5}$**, when the heating of **LI$_{2:5}$** was performed at 70 °C and 50% RH. Upon equilibrating under high humid conditions (RH

> 97% and 25 °C), both $\mathbf{LI}_{6:5}$ and $\mathbf{LI}_{4:3}$ crystals revert to $\mathbf{LI}_{2:5}$. (Supplementary Fig. S19c-d). These transformations among the three phases also resulted in significant alterations to their morphology (Supplementary Note S7, Supplementary Figs. S23,S24 and Supplementary Movies S1,S2), unit cell dimensions and volume (Fig. 4c), as well as the water sorption isotherms (Supplementary Fig. S25).

During these phase transitions, the dihedral angles (θ) underwent significant changes. In the sequence of transformations $\mathbf{LI}_{2:5} \rightarrow \mathbf{LI}_{4:3} \rightarrow \mathbf{LI}_{6:5}$, θ varied from -168.8° and 177.6° to 152.4°, 167.9°, 172.4°, and -175.5°, and further to -29.5°, -37.6°, and -177.9°, respectively (Fig. 4a). The $\boldsymbol{\chi}_1$ and $\boldsymbol{\chi}_2$ angles of **L** and **I** also vary among different values, most of which were observed in **LI**'s aqueous dispersed state from MD simulations (Supplementary Fig. S26). These observations suggest that side chain dynamics and a balanced H-bonding network are essential for lowering the energy barrier of such dramatic transformations in the solid state.

In addition, we also investigated the potential phase transformations of the $\mathbf{II}_{1:2}$ crystals (Fig. 4b). When heated up to 95 °C as observed in endothermic peaks at 40% RH, $\mathbf{II}_{1:2}$ crystals transformed to a polymorphic hydrate $\mathbf{II}_{1:2P}$ without any water loss (Fig 4b and Supplementary Figs. S27a,S28). During this transition, the hydrophobic columns in $\mathbf{II}_{1:2}$ transformed into nanochannels in $\mathbf{II}_{1:2P}$. Upon exposure to highly humid conditions (RH > 97% and 25 °C), $\mathbf{II}_{1:2P}$ underwent a phase transition back to the initial structure of $\mathbf{II}_{1:2}$ (Fig. 4b and Supplementary Fig. S27b). These transitions also resulted in changes in morphology, unit cell parameters, water sorption, and mechanical properties of the crystals of $\mathbf{II}_{1:2P}$ compared to $\mathbf{II}_{1:2}$ (Fig. 4c and Supplementary Figs. S29,S30). The Young's modulus changed from 6.3 GPa for $\mathbf{II}_{1:2}$ to 16.6 GPa for $\mathbf{II}_{1:2P}$ (Supplementary Fig. S31).

Phase-dependent mechanical properties of LI crystalline hydrates

Given the dramatic reconfiguration of **LI** from hexagonal to layered, along with changes in water contents, we investigated their mechanical properties using both AFM nanoindentation and simulations. The conformation changes of **LI** crystals significantly influence their mechanical properties (Fig. 5a-c, Supplementary Figs. S32, and Supplementary Note S4). As the crystal transformed and the water of crystallization decreased, we observed that Young's modulus of **LI** crystals reduced from 27.2 GPa (**LI$_{2:5}$**) to 10 GPa (**LI$_{4:3}$**) and then decreased significantly to 3.4 GPa (**LI$_{6:5}$**). To further investigate the molecular origins of these distinct mechanical properties, we performed DFTB simulations, where the obtained average values of Young's modulus agree with those obtained from the AFM nanoindentation, following the same order: **LI$_{2:5}$** > **LI$_{4:3}$** > **LI$_{6:5}$** (Fig. 5d-f, Supplementary Figs. S33-S36, Supplementary Note S8 and Supplementary Table S3).

Through simulations and crystal structures, we found that the honeycomb-like structure of **LI$_{2:5}$** exhibits similar moduli in different directions, with a maximum value of 22.2 GPa appearing along the water channel (Fig. 5g). However, when converting to **LI$_{6:5}$**, its van der Waals layer structure shows drastic variations in Young's modulus in different directions. The low value of Young's modulus (~0.6 GPa) is attributed to weak van der Waals interactions between the stacked layers along the direction perpendicular to the (001) plane (Fig. 5h), which results in observed low stiffness at the macroscale (Fig. 5b). As the crystal transformed to the other honeycomb-like **LI$_{4:3}$**, its Young's modulus showed similar values in all directions due to the symmetric arrangement of molecules (Fig. 5i). This finding illustrates the potential for developing smart materials whose mechanical properties can be modulated through subtle changes in water-material interactions with minimal energy input.

Phase-dependent photophysical properties of LI crystalline hydrates

These **LI** crystals also display phase-dependent fluorescence properties. Non-aromatic amino acids/peptides have previously been shown to exhibit intrinsic fluorescence typically induced by aggregation or nucleation of supramolecular assemblies[40,41]. The mechanism of this emission is thought to arise from specific interactions of H-bonding networks including short H-bonds leading to proton transfer[42] and constraints of the carbonyl groups[43]. We noted that, while the crystals of $\mathbf{IL_{11:10}}$, $\mathbf{LL_{7:6}}$, and $\mathbf{II_{1:2}}$ showed no significant emission (Supplementary Fig. S37), $\mathbf{LI_{2:5}}$ exhibited two intense peaks at $\lambda_{ex}/\lambda_{em}$ = 325/388 nm and $\lambda_{ex}/\lambda_{em}$ = 290/389 nm (Fig. 5j), and $\mathbf{LI_{6:5}}$ and $\mathbf{LI_{4:3}}$ only exhibited major peaks at $\lambda_{ex}/\lambda_{em}$ = 326/394 nm and $\lambda_{ex}/\lambda_{em}$ = 328/396 nm, respectively. The increase in intensity of the peak at $\lambda_{ex}/\lambda_{em}$ = 290/389 nm associated with the phase transitions is evident in the photographs of corresponding crystals under UV illumination, as $\mathbf{LI_{6:5}}$ and $\mathbf{LI_{4:3}}$ change their phases to $\mathbf{LI_{2:5}}$ (Fig. 5k-l and Supplementary Movies S3,S4).

We examined the electronic structure of the crystals to rationalize the difference in optical properties (Fig. 5m and Supplementary Fig. S38-S44). The electronic density of states revealed that the emitting structures exhibit lower band gaps with respect to the non-emitting structures (Fig. 5n and Supplementary Figs. S38-S43). These results qualitatively align with the slight red shift observed in the maximum excitation wavelength for the **LI** systems. Delving into the electronic transitions, we observe that the highest occupied molecular orbital (HOMO) is an *n*-orbital involving the COO^- and CO groups, while the lowest unoccupied molecular orbital (LUMO) exhibits a π^* character mostly localized on the amide bond (Fig. 5m and Supplementary Fig. S44). Since peptide-peptide and peptide-water interactions occur through these functional groups, H-bonds play a significant role in the lowest absorption ($n \rightarrow \pi^*$) transitions. Previous studies have shown that strong H-bond interactions near the COO^- and CO groups can constrain the non-radiative relaxation pathways, enabling fluorescence in these systems[43]. The fluorescent systems, $\mathbf{LI}_{2:5}$, $\mathbf{LI}_{6:5}$, and $\mathbf{LI}_{4:3}$, have a higher number of both types of H-bonds, particularly within the shorter distance regions (1.8-2.2 A) (Supplementary Fig. S45), than the non-fluorescent systems (Supplementary Fig. S46). Compared to the non-fluorescent systems, this feature may hinder the extension of carbonyl bond upon excitation.

Our results illustrate how the dynamic nature of aliphatic side-chain interactions known in solution-state proteins can be harnessed to develop simultaneously stable and reconfigurable materials in the solid state. It is clear that the side-chain interactions of amino acids play an important role in balancing backbone, side-chain, and water interactions, leading to dynamic conformations in dispersed solution states and solids. Moreover, our findings suggest that the water-stabilized supramolecular structures become more prone to reconfiguration when alternate branched structures with varying rotamers of aliphatic moieties are considered. This results from the synergistic interplay between aliphatic and water-driven H-bonds, as well as internal rotational entropy enabling precise tuning of material properties. By combining these aliphatic interactions with directional aromatic and H-bonding interactions, we envision new design principles that will significantly enhance our ability to develop reconfigurable materials to complement the static and stable structures demonstrated, thus opening up opportunities for adaptive functions, potentially surpassing those found in biological systems.

Methods:

Materials and crystal preparation: Dipeptides **LI**, **IL**, **II,** and **LL** were purchased from Bachem. Potassium hydroxide, magnesium chloride, sodium bromide, sodium chloride, and potassium chloride, used for preparing saturated salt solutions to regulate relative humidity (RH), were purchased from Sigma Aldrich. The purity of the peptides was assessed using Liquid Chromatography–Mass Spectrometry (ThermoFisher Scientific). To ensure the absence of trifluoroacetic acid (TFA), a common impurity from synthesis, ^{19}F NMR measurements were performed on a D_2O solution of the dipeptides using an Avance III 300 MHz NMR spectrometer (Bruker). The absence of peaks in the ^{19}F NMR spectrum indicated that no TFA was present.

Crystals of the dipeptides **LI**, **IL**, **II**, and **LL** were obtained by evaporating a saturated aqueous solution of the corresponding dipeptide in an RH-controlled chamber maintained at approximately 80% RH and 25 °C. Notably, the crystallization of **LI** using this method produced the pure polymorph $\mathbf{LI}_{2:5}$ without the need for the additive D-leucine, contrasting a previous report[44]. Using the same method, **LL** and **IL** formed needle-like crystals of $\mathbf{LL}_{7:6}$ and $\mathbf{IL}_{11:10}$, while **II** and **LI** resulted in pyramidal or cuboidal crystals of $\mathbf{II}_{1:2}$ and $\mathbf{LI}_{2:5}$, respectively (Supplementary Fig.S7).

Phase transitions of dipeptide crystals: The phase transitions of **LI** and **II** crystals were achieved by controlling RH and temperature. For **LI** crystals, the $\mathbf{LI}_{2:5}$ crystals were first equilibrated under humid conditions for 24 hrs by placing a 2 mL vial containing 2 mg of $\mathbf{LI}_{2:5}$ crystals inside another 20 mL vial that was one-quarter filled with deionized water. To control RH at various temperatures, separate 20 mL vials were prepared, each filled one-quarter with the appropriate saturated salt solution needed to achieve the desired RH level[45]. For $\mathbf{LI}_{2:5}$ to $\mathbf{LI}_{6:5}$, $\mathbf{LI}_{2:5}$ to $\mathbf{LI}_{4:3}$, and $\mathbf{LI}_{4:3}$ to $\mathbf{LI}_{6:5}$ transitions, vials containing saturated NaBr salt solution were sealed and heated at appropriate temperatures for 3 hrs (55 °C for **LI$_{2:5}$** to **LI$_{6:5}$** transition, 60 °C for **LI$_{2:5}$** to **LI$_{4:3}$** transition, and 70 °C for **LI$_{4:3}$** to **LI$_{6:5}$** transitions). Then, the **LI$_{2:5}$** crystals were transferred to these pre-heated vials containing the NaBr saturated salt solutions, 2 μL of water was added, and the vials were sealed immediately. After heating (2 hrs for **LI$_{2:5}$** to **LI$_{6:5}$** transition, 30 min for **LI$_{2:5}$** to **LI$_{4:3}$** transition, 45 min for **LI$_{4:3}$** to **LI$_{6:5}$** transitions), the vials were quickly cooled in a water bath at 25 °C. Although the transformation of **LI$_{4:3}$** to **LI$_{6:5}$** happened right after the transition from **LI$_{2:5}$** to **LI$_{4:3}$**, this transformation did not occur when starting with dry **LI$_{4:3}$** crystals under the same conditions. The transitions from **LI$_{4:3}$** to **LI$_{2:5}$** and from **LI$_{6:5}$** to **LI$_{2:5}$** were achieved by placing the initial crystals under humid conditions (>97% RH). For **II** crystals, the dry crystals of **II$_{1:2}$** were heated in an open vial at 95 °C and ~40% RH. **II$_{1:2P}$** to **II$_{1:2}$** transition was achieved by placing the initial crystals under humid conditions (>97% RH).

Solubility measurements**:** To measure the solubility, we prepared peptide suspensions/solutions in 500 μL of deionized water with increasing concentrations from 0.1 M to 1 M at 25 °C. Each of these suspensions was subjected to three cycles of heating (at 90 °C) followed by sonication and then rapidly cooled to 25 °C by placing them in a water bath. After equilibration at 25 °C for 5 minutes, the vials were examined under a microscope for precipitation or crystallization. The concentration of the peptide solution right below the point at which precipitation or crystallization occurs is considered solubility. The experiments were repeated three times at concentrations near the solubility limits.

All-atom molecular dynamics (MD) simulations: MD simulations were performed using GROMACS 2022.5[46]. PDB files for the all-atom dipeptide structures (**FF**, **II**, **LL**, **LI**, and **LL**) were generated using PyMOL 2.5.0. These files were processed using the GROMACS's *gmx pdb2gmx* tool to create atomistic topologies with zwitterionic termini in the CHARMM36m force field[47,48]. Subsequently, 140 dipeptides were randomly inserted into a cubic box (using *gmx* *insert-molecules*) with an edge length of 7 nm, yielding an approximate peptide concentration of 0.66 M. The box configuration was then solvated with explicit TIP3P water molecules and subjected to steepest-descent energy minimization until forces converged below 1000.0 kJ/mol/nm. Packing conflicts were resolved, and the system was equilibrated at 298 K and 1.0 bar using short consecutive *NVT* and *NPT* equilibrations for 5000 steps using a timestep of 2 fs. Temperature coupling was achieved using the V-rescale algorithm[49] (modified Berendsen thermostat) with a time constant of 0.1 ps, while pressure coupling was maintained isotopically with a Parrinello-Rahman barostat at a time constant of 2.0 ps[50]. The heavy atoms of the peptides were positioned and restrained during equilibration before the production runs. Triplicate 1000 ns (1 µs) molecular dynamics simulations were performed for each of the five dipeptide sequences using the leap-frog MD integrator. van der Waals interactions were treated with a force-switch algorithm, using a short-range cutoff of 1.2 nm and a switching distance of 1.0 nm. Electrostatics were treated with Particle Mesh Ewald (PME) with a short-range cutoff of 1.2 nm. Bonds were constrained using the LINCS (Linear Constraint Solver) algorithm[51]. Trajectory frames were saved every 50 ps (25,000 steps), resulting in 20,000 frames per trajectory for subsequent analysis and characterization of dipeptide dynamics and interactions.

Changes to the Solvent Accessible Surface Area (SASA) during the equilibrations were evaluated using the GROMACS tool *gmx sasa*, with a fixed solvent probe radius of 0.14 nm. The SASA data were converted to aggregation propensity (AP) using a custom Python script based on the following equation, Eqn. S1:

$$AP = \frac{SASA_{initial\ frame\ at\ t=0}}{SASA_{frame\ at\ t\geq 0}} \tag{S1}$$

Accessible Surface Areas (ASA) in nm^2 were calculated for the various side chains in the dipeptides by varying the probe size from 1 Å and 15 Å in 1 Å increments. Pairwise H-bonding interactions between the peptide backbones and water were analyzed from the trajectories using *gmx bond*, with a donor-acceptor distance cutoff of 0.35 nm and an angle cutoff of 30°.

The side chain dihedral angles χ_1 and χ_2 for the aliphatic dipeptides were measured over the last 100 ns of simulations using 'gmx chi'. Initially, these angles were computed individually for each residue (first and second) of the dipeptides and combined to create χ_1 - χ_2 Ramachandran Plots. Normalized histograms of these dihedral angle populations were generated for all residues of each type across the 140 simulated dipeptides. The dihedral angles, θ, were measured for the self-assembled structures and single peptide simulations for the CB(1)-CA(1)-CA(2)-CB(2) atoms using a custom VMD tcl script. The analysis focused on the last 100 ns of each trajectory, encompassing 2000 frames per trajectory, to ensure statistical reliability post-equilibration. For visualization and trajectory rendering, VMD 1.9.3 was used[52].

Dynamic vapor sorption (DVS): DVS measurements of the dipeptide crystals were conducted using the DVS Intrinsic PLUS (Surface Measurement Systems). 5 mg crystals of phase-pure polymorphs of the dipeptides were loaded into an 18 mm sample metal pan (DVS Intrinsic/Endeavour), and the mass change was recorded in real-time as the RH varied between 10% and 95%. During the test, the RH was increased to the next level when the mass change rate (dm/dt) stabilized at 0.05 mg/min for 5 minutes or when the same RH was maintained for 20 min. Hydration/dehydration cycles were performed in triplicate.

Atomic force microscope (AFM): The topography and stiffness of the crystals were measured using a Bruker MultiMode 8 AFM (Bruker) equipped with a RH-controlled chamber. The crystals were deposited onto a glass substrate (0.5 mm x 0.5 mm), and the RH within the chamber was regulated by mixing dry laboratory-grade air with water-saturated air in the appropriate proportions. A commercial RH sensor (HIH-4021-003, HONEYWELL) positioned near the sample monitored the RH. Throughout the experiments, the RH and temperature were maintained at 50% RH and 25 °C conditions, under which all polymorphs remained stable for extended periods. An AFM probe with a tip radius of approximately 2 nm (SCANASYST-AIR, Bruker) was used to measure changes in crystal topography. AFM nanoindentation was performed to assess crystal stiffness using a probe with a tip radius of around 8 nm (NCHV, Bruker). Force-indentation curves were recorded and analyzed using Nanoscope 1.9 software (Bruker). Young's modulus (*E*) of the crystals was calculated using the Hertz model (Eqn. S2):

$$F = \frac{4}{3}\left(\frac{E}{1-v^2}\right) R_{tip}^{\frac{1}{2}} h^{2/3} \tag{S2}$$

where *F* is the force applied, *v* is Poisson's ratio, R_{tip} is the radius of the tip, and *h* is the nanoindentation depth. The reported values are an average of 15 measurements.

<u>Differential scanning calorimetry (DSC) and thermo-gravimetric analysis (TGA)</u>: DSC and TGA were performed using a DSC-TGA Q600 SDT (TA Instruments). Approximately 3 mg of crystals were loaded into a Tzero aluminum pan. The scanning process involved heating from 25°C to 200 °C at a rate of 5°C/min under a N_2 purge flowing at 50 mL/min.

<u>Powder X-ray diffraction (PXRD)</u>: The PXRD measurements were conducted using an X'Pert Pro diffractometer (Malvern Panalytical). The crystals were ground in a mortar and deposited onto a glass slide. The X-ray source (Philips) was a high-intensity ceramic sealed Cu tube operating at 3 kW, emitting radiation with a wavelength of 1.5405 Å. A Ni filter was positioned in the path of the diffracted beam before reaching the detector (PIXcel1D). To control the RH near the sample during measurements, a custom-made acrylic tube with small windows covered by 0.6-micron-thick Mylar sheets was used. This setup facilitated the unobstructed passage of X-rays while maintaining controlled RH. A mixture of dry and humid air, adjusted to the appropriate proportions, was circulated through the acrylic holder using thin tubes, and the RH

values were monitored with an RH sensor (HIH-4021-003, Honeywell) positioned near the sample. The sample was allowed to equilibrate to the desired RH for at least 15 minutes before conducting the diffraction measurement. PXRD measurements of all crystals $\mathbf{LI_{2:5}}$, $\mathbf{II_{1:2}}$, $\mathbf{II_{1:2P}}$, $\mathbf{IL_{11:10}}$, $\mathbf{LL_{7:6}}$, $\mathbf{LI_{6:5}}$, and $\mathbf{LI_{4:3}}$ was performed at 50% RH and 25 °C. For measurements involving phase transformations between phases $\mathbf{LI_{2:5}}$ and $\mathbf{LI_{unk}}$, the RH was varied between 10% and 90% by adjusting the dry-to-humid air ratio in the circulating mixture.

Single-crystal X-ray diffraction: The single-crystal X-ray diffraction data were collected using a Bruker D8 VENTURE diffractometer (Bruker) with Cu Kα radiation as the source. Details regarding crystal data, data collection, and refinement parameters are summarized in Supplementary Table S1. The structure was solved using a dual-space method and standard difference map techniques, followed by refinement using full-matrix least-squares procedures on F^2 with SHELXTL (Version 2018/3)[53]. Hydrogen atoms bonded to carbon atoms were placed in calculated positions and refined using a riding model [$U_{\mathrm{iso}}(\mathrm{H}) = 1.2–1.5U_{\mathrm{eq}}(\mathrm{C})$]. Hydrogen atoms attached to nitrogen or oxygen were located on the difference map, and their positions were freely refined using DFIX and/or DANG restraints as needed [$U_{\mathrm{iso}}(\mathrm{H}) = 1.2U_{\mathrm{eq}}(\mathrm{N}$ or $\mathrm{O})$]. The crystal structures were analyzed and visualized using Mercury 2021.3.0[54]. SQUEEZE/PLATON[55] was used to investigate the solvent-accessible void, but no electron density was found, indicating that the void is not occupied.

Environmental scanning electron microscopy (ESEM): ESEM was performed using Quattro ESEM (Thermofisher Scientific). Crystals of $\mathbf{LI_{2:5}}$ were initially grown on glass slides (0.5 mm x 0.5 mm) and subsequently transformed into $\mathbf{LI_{6:5}}$ and $\mathbf{LI_{4:3}}$ under appropriate conditions. These samples were loaded into the ESEM with a Peltier cooling stage, maintaining the sample temperature at 1 °C. RH was modulated between 30% and 100% by adjusting chamber vacuum pressures (200 Pa to 700 Pa). The working distance was maintained in the range of 5.5 mm to 6.1

mm during the analysis. A gaseous secondary electron detector (GSED) captured secondary electrons, producing detailed electron micrographs from multiple regions of each sample at various magnifications and resolutions. High voltage settings of 5 or 10 kV and currents from 64 pA to 0.42 nA were utilized. Adjustments to contrast and brightness were made to enhance image quality, allowing for a thorough examination of the samples' morphology and microstructural features.

Computation methodology for elastic constant predictions: Elastic constants for each hydrate crystal were computed using Density Functional based Tight Binding (DFTB)[56], specifically implemented in the DFTB+ code[57] with the 3ob-3-1 parameter set (http://www.dftb.org)[58]. DFTB is a semi-empirical electronic structure method that expresses the Hamiltonian with a suitable balance between rigorous quantum mechanics and empirical approximation, making it effective for complex organic crystals[59]. In our DFTB calculation, we employed the self-consistent charge (SCC) method[60] with a convergence criterion of $1e^{-6}$ atomic units. To account for van der Waals dispersion effects, we applied both the Tkatchenko-Scheffler[61] and D3[62]correction schemes. We explored a range of strained configurations for each crystal to accurately derive the stress-strain relationship, taking their crystal symmetry into account, and derived the elastic constants. To analyze the anisotropic behavior of crystal packing and elastic properties, we utilized the ELATE[63] and PyXtal[64]codes. All scripts used in this work are publicly available at https://github.com/MaterSim/PyXtal_DFTB. The average values of elastic moduli along with corresponding plots (Supplementary Figs. S12-S17 and S33-S36) can be accessed by entering the computed elastic constants matrix (Supplementary Table S2) at ELATE program: https://progs.coudert.name/elate.

Fluorescence spectroscopy: 3D fluorescence contour plots were recorded using an FP-8500 Fluorometer (Jasco), featuring excitation versus emission scans. Both excitation and emission spectra were recorded with a bandwidth of 2.5 nm, a response time of 0.1 sec, and a data collection rate of 1000 nm/min. Emission spectra were measured at 0.1 nm intervals, while excitation spectra were recorded at 1 nm intervals. Samples were prepared as fine powders to enhance adhesion to the 0.5 mm thick CaF_2 substrate. The CaF_2 discs containing the samples were placed in a custom closed chamber equipped with an inlet and outlet for humid air. RH was monitored using an RH sensor (HIH-4021-003, Honeywell), maintaining the RH at 50% RH during all the measurements.

Computation of electronic structure of dipeptide crystals: The geometries of all crystal structures were initially optimized using plane-wave density functional theory (DFT) as implemented in the Quantum Espresso package[65-67]. The Broyden-Fletcher-Goldfarb-Shanno quasi-Newton algorithm[68-71] was employed, with convergence thresholds set at 1.0×10^{-4} Ry for energy and 3.9×10^{-4} Ry/Bohr for force. The kinetic energy cutoff for wavefunctions and charge density were set to 75 Ry and 300 Ry, respectively. We utilized the optimized norm-conserving Vanderbilt (ONCV) pseudopotentials proposed by Hamann[72], and the Brillouin zone was sampled with a Γ k-point grid. The initial optimizations were performed with the generalized gradient approximation, specifically the Perdew-Burke-Ernzerhof (PBE) exchange-correlation (xc) functional[73]. The relaxed structures were subsequently refined using the more accurate hybrid PBE0 xc functional[74].

Following the geometry optimizations, we calculated the band gap and the total projected density of states (PDOS) (Supplementary Figs. S38-S43) for each crystal structure using Quantum Espresso[65-67], maintaining the same kinetic energy cutoff values and ONCV pseudopotentials. Since the calculations were performed on optimized structures, thermal vibrations, and nuclear quantum effects, which could affect the quantities of interest, were not considered. All electronic structure calculations were conducted with the PBE0 xc functional, employing a Gaussian broadening of 0.005 Ry for the PDOS plots. The frontier orbitals, specifically the highest occupied molecular orbital (HOMO) and the lowest unoccupied molecular orbital (LUMO) (Supplementary Fig. S44), were computed using a post-processing tool in Quantum Espresso and visualized with VMD software[52].

Acknowledgments: This work is supported in part by the Army Research Office (Grant No. W911NF-21-1-0172), National Science Foundation (Grant No. CBET-2238129, DMR-2410178), Office of Naval Research for the Vannevar Bush Faculty Fellowship (RVU) (Grant No. N00014-21-1-2967), and Air Force Office of Scientific Research (MCN) (Grant No. FA9550-20-1-0158). We thank Darjan Podbevšek for customizing a humidity chamber used during the PXRD measurements.

Author contributions: X.C. and R.V.U. conceived and initiated the project. V.A. grew all the dipeptide crystals, performed PXRD, DSC, TGA, fluorescence measurements, analyzed the data and crystal structures. E.N. performed AFM measurements and analyzed the data. D.D. performed MD simulations. O.G.R., D.A.A.R. and Q.Z. performed DFTB studies on crystal structures to compute the Young's modulus. G.D.M., D.B., M.M. and A.H. conducted theoretical studies on solid-state fluorescence of dipeptides. M.C.N. conducted SC-XRD experiments and solved single crystal structures. S.Z. performed ESEM measurements. V.A., R.V.U. and X.C. wrote the paper. V.A. and X.C. prepared the visualizations. R.V.U. and X.C. supervised the project.

Competing interests: Authors declare no competing interests.

Data and materials availability: Crystal structures of **LI$_{6:5}$** and **II$_{1:2P}$** were deposited to Cambridge Crystallographic Data Centre (CCDC, https://www.ccdc.cam.ac.uk) under the deposition numbers 2387164 and 2387165, respectively. All other data are available in the main text or the supplementary information.

References

1. Zhu, J. et al. Protein Assembly by Design. *Chem. Rev.* **121**, 13701–13796 (2021).
2. Aida, T., Meijer, E. W. & Stupp, S. I. Functional supramolecular polymers. *Science* **335**, 813–817 (2012).
3. Zhang, S. Fabrication of novel biomaterials through molecular self-assembly. *Nat. Biotechnol.* **21**, 1171–1178 (2003).
4. Pappas, C. G. *et al*. Dynamic peptide libraries for the discovery of supramolecular nanomaterials. *Nat. Nanotechnol.* **11**, 960–967 (2016).
5. Yang, W. Y., Ahn, J. H., Yoo, Y. S., Oh, N. K. & Lee, M. Supramolecular barrels from amphiphilic rigid–flexible macrocycles. *Nat. Mater.* **4**, 399–402 (2005).
6. Yuan, C. *et al*. High-entropy non-covalent cyclic peptide glass. *Nat. Nanotechnol.*​**19**, 1840–1848 (2024).
7. Gazit, E. Aromatic dipeptides light up. *Nat. Nanotechnol.* **11**, 309–310 (2016).
8. Tadepalli, S., Slocik, J. M., Gupta, M. K., Naik, R. R. & Singamaneni, S. Bio-Optics and Bio-Inspired Optical Materials. *Chem. Rev.* **117**, 12705–12763 (2017).
9. Finkelstein-Zuta, G. *et al.* A self-healing multispectral transparent adhesive peptide glass. *Nature* **630**, 368–374 (2024).
10. Azuri, I., Adler-Abramovich, L., Gazit, E., Hod, O. & Kronik, L. Why are diphenylalanine-based peptide nanostructures so rigid? Insights from first principles calculations. *J. Am. Chem. Soc*. **136**, 963–969 (2014).
11. Piotrowska, R. et al. Mechanistic insights of evaporation-induced actuation in supramolecular crystals. *Nat. Mat.* **20**, 403–409 (2020).
12. Sheehan, F. K. et al. Aromatic Zipper Topology Dictates Water-Responsive Actuation in Phenylalanine-Based Crystals. *Small* **19**, 2207773 (2023).

13. Garcia, A. M. et al. Chirality Effects on Peptide Self-Assembly Unraveled from Molecules to Materials. *Chem* **4**, 1862–1876 (2018).

14. Álvarez, Z. et al. Bioactive scaffolds with enhanced supramolecular motion promote recovery from spinal cord injury. *Science* **374**, 848–856 (2021).

15. Yang, Y., Sai, H., Egner, S. A., Qiu, R., Palmer, L. C. & Stupp, S. I. Peptide programming of supramolecular vinylidene fluoride ferroelectric phases. *Nature* **634**, 833–841 (2024).

16. Rabone, J. et al. An adaptable peptide-based porous material. *Science* **329**, 1053–1057 (2010).

17. Sugase, K., Dyson, H. J. &. Wright, P. E. Mechanism of coupled folding and binding of an intrinsically disordered protein. *Nature* **447**, 1021–1025 (2007).

18. Tesei, G. et al. Conformational ensembles of the human intrinsically disordered proteome. *Nature* **626**, 897–904 (2024).

19. Najmanovich, R., Kuttner, J., Sobolev, V. & Edelman, M. Side-Chain Flexibility in Proteins Upon Ligand Binding. *Proteins* **39**, 261–268 (2000).

20. Hansen, D. F., Neudecker, P., Vallurupalli, P., Mulder, F. A. A. & Kay, L. E. Determination of Leu side-chain conformations in excited protein states by NMR relaxation dispersion. *J. Am. Chem. Soc.* **132**, 42–43 (2010).

21. Hansen, D. F., Neudecker, P. & Kay, L. E. Determination of isoleucine side-chain conformations in ground and excited states of proteins from chemical shifts. *J. Am. Chem. Soc.* **132**, 7589–7591 (2010).

22. Caballero, D., Smith, W. W., O'Hern, C. S. & Regan, L. Equilibrium transitions between side-chain conformations in leucine and isoleucine. *Proteins* **83**, 1488–1499 (2015).

23. Schrauber, H., Eisenhaber, F. & Argos, P. Rotamers: To be or not to be?: An Analysis of Amino Acid Side-chain Conformations in Globular Proteins. *J. Mol. Biol*. **230**, 592–612 (1993).

24. O'Shea, E. K., Klemm, J. D., Kim, P. S. & Alber, T. X-Ray Structure of the GCN4 Leucine Zipper, a Two-Stranded, Parallel Coiled Coil. *Science* **254**, 539–544 (1991).

25. Wagner, J. P., Schreiner, P. R., Schreiner, P. R. & Wagner, J. P. London Dispersion in Molecular Chemistry—Reconsidering Steric Effects. *Angew. Chem. Int. Ed*. **54**, 12274–12296 (2015).

26. Doig, A. J. Thermodynamics of amino acid side-chain internal rotations. *Biophys. Chem.* **61**, 131–141 (1996).

27. Chakrabarti, P. & Bhattacharyya, R. Geometry of nonbonded interactions involving planar groups in proteins. *Prog. Biophys. Mol. Biol*. **95**, 83–137 (2007).

28. Lakshmanan, A. et al. Aliphatic peptides show similar self-assembly to amyloid core sequences, challenging the importance of aromatic interactions in amyloidosis. *Proc. Natl. Acad. Sci. U S A*. **110**, 519–524 (2013).

29. Ksovreli, M. et al. Leucine-Based Pseudo-Proteins (LPPs) as Promising Biomaterials: A Study of Cell-Supporting Properties. *Polymers* **15**, 3328 (2023).

30. Pramod, T., Khazeber, R., Athiyarath, V. & Sureshan, K. M. Topochemistry for Difficult Peptide–Polymer Synthesis: Single-Crystal-to-Single-Crystal Synthesis of an Isoleucine-Based Polymer, a Hydrophobic Coating Material. *J. Am. Chem. Soc.* **146**, 7257–7265 (2024).

31. Rufo, C. M. et al. Short peptides self-assemble to produce catalytic amyloids. *Nat. Chem.* **6**, 303–309 (2014).

32. Reches, M., & Gazit, E. Casting metal nanowires within discrete self-assembled peptide nanotubes. *Science* **300**, 625–627 (2003).

33. C. H. Görbitz, Microporous organic materials from hydrophobic dipeptides. *Chem. Eur. J.* **13**, 1022–1031 (2007).

34. Bera, S. et al. Solid-state packing dictates the unexpected solubility of aromatic peptides. *Cell Rep. Phys. Sci*. **2**, 100391 (2021).

35. Frederix, P. W. J. M., Ulijn, R. V., Hunt, N. T. & Tuttle, T. Virtual screening for dipeptide aggregation: Toward predictive tools for peptide self-Assembly. *J. Phys. Chem. Lett.* **2**, 2380–2384 (2011).

36. Waters, M. L. Aromatic interactions in peptides: Impact on structure and function. *Biopolymers*, **76**, 435–445 (2004).

37. Görbitz, C. H. Hydrophobic dipeptides: the final piece in the puzzle. *Acta Crystallogr. B Struct. Sci. Cryst. Eng. Mater.* **74**, 311–318 (2018).

38. Görbitz, C. H. Nanotube Formation by Hydrophobic Dipeptides. *Chem. Eur. J.* **7**, 5153–5159 (2001).

39. Elstner, M. et al. Self-consistent-charge density-functional tight-binding method for simulations of complex materials properties. *Phys. Rev.* **B58**, 7260 (1998).

40. Zhang, H. et al. Clusterization-triggered emission: Uncommon luminescence from common materials. *Mater. Today* **32**, 275–292 (2020).

41. Chen, X. *et al.* Prevalent intrinsic emission from nonaromatic amino acids and poly(amino acids). *Sci. China Chem*. **61**, 351–359 (2018).

42. Stephens, A. D. *et al.* Short hydrogen bonds enhance nonaromatic protein-related fluorescence. *Proc. Natl. Acad. Sci. U S A.* **118**, e2020389118 (2021).

43. Mirón, G. D. *et al.* The carbonyl-lock mechanism underlying non-aromatic fluorescence in biological matter. *Nat. Commun*. **14**, 1–13 (2023).

44. Görbitz, C. H. & Rise, F. Template-directed supramolecular assembly of a new type of

nanoporous peptide-based material. *J. Pept. Sci.* **14**, 210–216 (2008).

45. Greenspan, L. Humidity Fixed Points of Binary Saturated Aqueous Solutions. *J. Res. Natl. Bur. Stand. Sect. A, Phys. Chem.* **81A**, 89 (1977).
46. Abraham, M. J. et al. GROMACS: High performance molecular simulations through multi-level parallelism from laptops to supercomputers. *SoftwareX* **1–2**, 19–25 (2015).
47. Huang, J. et al. CHARMM36m: an improved force field for folded and intrinsically disordered proteins. *Nat. Methods 2016 141* **14**, 71–73 (2016).
48. Lindahl, E., Bjelkmar, P., Larsson, P., Cuendet, M. A. & Hess, B. Implementation of the CHARMM Force Field in GROMACS: Analysis of Protein Stability Effects from Correction Maps, Virtual Interaction Sites, and Water Models. *J. Chem. Theory Comput.* **6**, 459–466 (2010).
49. Bussi, G., Donadio, D. & Parrinello, M. Canonical sampling through velocity rescaling. *J. Chem. Phys.* **126** (2007).
50. Parrinello, M. & Rahman, A Polymorphic transitions in single crystals: A new molecular dynamics method. *J. Appl. Phys.* **52**, 7182–7190 (1981).
51. Hess, B. P-LINCS: A Parallel Linear Constraint Solver for Molecular Simulation. *J. Chem. Theory Comput.* **4**, 116–122 (2007).
52. Humphrey, W., Dalke, A. & Schulten, K. VMD: Visual molecular dynamics. *J. Mol. Graph.* **14**, 33–38 (1996).
53. Sheldrick, G. M. SHELXT – Integrated space-group and crystal-structure determination. *Acta Cryst*. **A71**, 3–8 (2015).
54. MacRae, C. F. et al. Mercury 4.0: from visualization to analysis, design and prediction. *J. Appl. Crystallogr.* **53**, 226–235 (2020).
55. Spek, A. L. PLATON, A Multipurpose Crystallographic Tool, Utrecht University, Utrecht,

The Netherlands. (2005).

56. Elstner, M. et al. Self-consistent-charge density-functional tight-binding method for simulations of complex materials properties. *Phys. Rev. B* **58**, 7260 (1998).
57. Hourahine, B. et al. DFTB+, a software package for efficient approximate density functional theory based atomistic simulations. *J. Chem. Phys.* **152**, 124101 (2020).
58. Gaus, M., Goez, A. & Elstner, M. Parametrization and benchmark of DFTB3 for organic molecules. *J. Chem. Theory Comput.* **9**, 338–354 (2013).
59. Brandenburg, J. G. & Grimme, S. Accurate modeling of organic molecular crystals by dispersion-corrected density functional tight binding (DFTB). *J. Phys. Chem. Lett.* **5**, 1785–1789 (2014).
60. Gaus, M., Cui, Q. & Elstner, M. DFTB3: Extension of the self-consistent-charge density-functional tight-binding method (SCC-DFTB). *J. Chem. Theory Comput.* **7**, 931–948 (2011).
61. Tkatchenko, A., Distasio, R. A., Car, R. & Scheffler, M. Accurate and efficient method for many-body van der Waals interactions. *Phys. Rev. Lett.* **108**, 236402 (2012).
62. Grimme, S., Antony, J., Ehrlich, S. & Krieg, H. A consistent and accurate ab initio parametrization of density functional dispersion correction (DFT-D) for the 94 elements H-Pu. *J. Chem. Phys.* **132** (2010).
63. Gaillac, R., Pullumbi, P. & Coudert, F. X. ELATE: an open-source online application for analysis and visualization of elastic tensors. *J. Phys. Condens. Matter* **28**, 275201 (2016).
64. Fredericks, S., Parrish, K., Sayre, D. & Zhu, Q. PyXtal: A Python library for crystal structure generation and symmetry analysis. *Comput. Phys. Commun.* **261**, 107810 (2021).
65. Giannozzi, P. et al. QUANTUM ESPRESSO: A modular and open-source software project for quantum simulations of materials. *J. Phys. Condens. Matter* **21**, 395502 (2009).
66. Giannozzi, P. et. al. Advanced capabilities for materials modelling with Quantum

ESPRESSO. *J. Phys. Condens. Matter* **29**, 465901 (2017).

67. Giannozzi, P. et. al. Quantum ESPRESSO toward the exascale. *J. Chem. Phys.* **152** (2020).
68. Broyden, C. G. The Convergence of a Class of Double-rank Minimization Algorithms 1. General Considerations. *IMA J. Appl. Math.* **6**, 76–90 (1970).
69. Fletcher, R. A new approach to variable metric algorithms. *Comput. J.* **13**, 317–322 (1970).
70. Goldfarb, D. A family of variable-metric methods derived by variational means. *Math. Comput.* **24**, 23–26 (1970).
71. Shanno, D. F. Conditioning of quasi-Newton methods for function minimization. *Math. Comput.* **24**, 647–656 (1970).
72. Hamann, D. R. Optimized norm-conserving Vanderbilt pseudopotentials. *Phys. Rev. B - Condens. Matter Mater. Phys.* **88**, 085117 (2013).
73. Perdew, J. P., Burke, K., & Ernzerhof, M. Generalized Gradient Approximation Made Simple. *Phys. Rev. Lett.* **77**, 3865 (1996).
74. Adamo, C., Barone, V., Adamo, C., & Barone, V. Toward reliable density functional methods without adjustable parameters: The PBE0 model. *J. Chem. Phys.* **110**, 6158–6170 (1999).

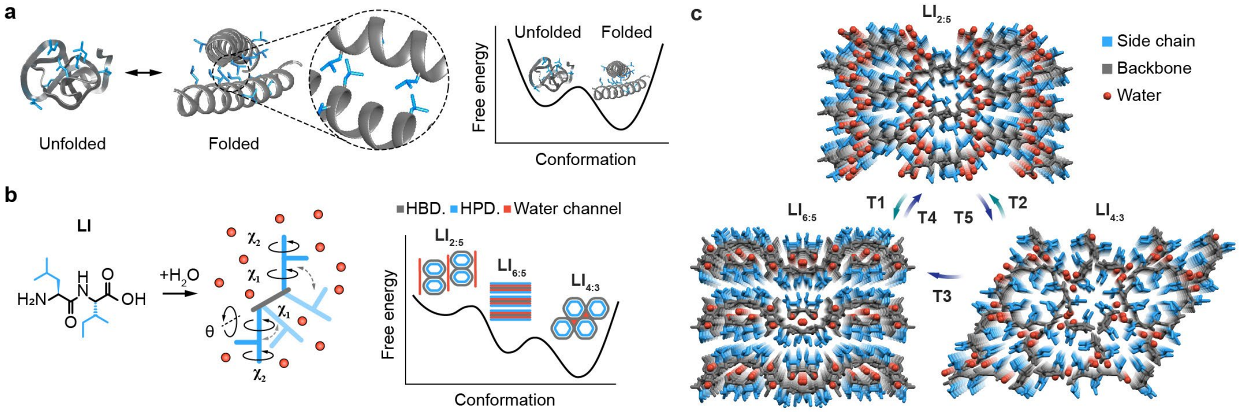

Fig. 1 | Protein dynamics inspired design of peptide crystals with context-adaptive topology. **a**, Schematic illustration of the conformational flexibility of a protein through its free energy landscapes. The coiled coil protein, GCN4 leucine zipper[24] is used as an example. **b**, **LI** dipeptide with various side chain dihedral angles $\boldsymbol{\chi}_1$ and $\boldsymbol{\chi}_2$, and backbone angle θ, enabling the solid-state phase transformations between three energy states. The cartoon in the plot represents various topologies adopted by **LI** crystals, highlighting the changes in relative orientations of the nanoscale hydrophobic domains (colored in blue) and hydrophilic water channels (colored in red). **c**, Crystal structures of three interconvertible **LI** hydrates (**T1-T5** represent phase transition conditions with **T1** = 55 °C/50% RH, **T2** = 60 °C/50% RH, **T3** = 70 °C/50% RH, **T4** and **T5** = 25 °C/> 97 % RH).

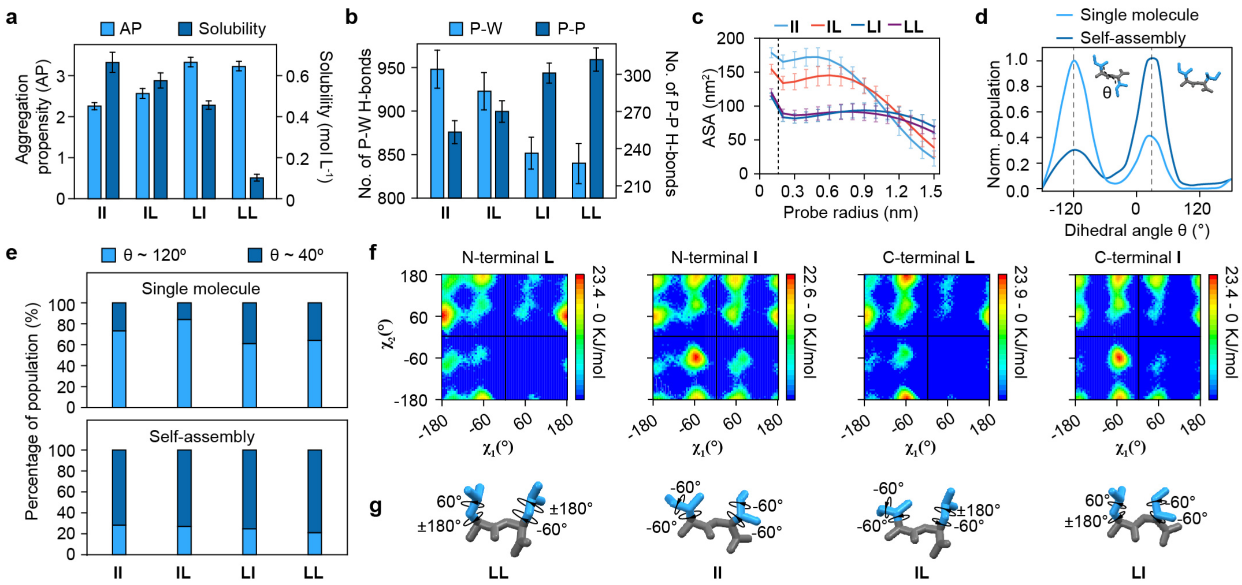

Fig. 2 | Aliphatic side chain dynamics of L and I of dipeptides in aqueous dispersions. a, Aggregation propensity (AP) and solubilities of **L** and **I** dipeptides. **b**, The number of peptide-water (P-W) and peptide-peptide (P-P) H-bonds in dipeptide dispersions. **c**, Accessible surface area (ASA) *vs.* probe radius quantifying the accessibility of the dipeptide side chains to simulated probes of various dimensions within simulated dispersions. The dotted lines represent the probe radius corresponding to the van der Waals radius of a water molecule. **d**, The probability distribution of the dihedral angle θ of dipeptide **II** when it is in both single molecule and self-assembled states. Plots for other dipeptides are provided in Supplementary Fig. S3. **e**, The relative populations of dipeptides adopting two major θ of ~120° and ~ 40° at the single molecule and self-assembly states. **f**, 2D plots depicting χ_1/ χ_2 presented as Ramachandran plots for the N-terminal and C-terminal residues **L** and **I**, of dipeptides. **g**, Schematic of the most probable dipeptide conformations in multi-molecule dispersions obtained from the MD simulation.

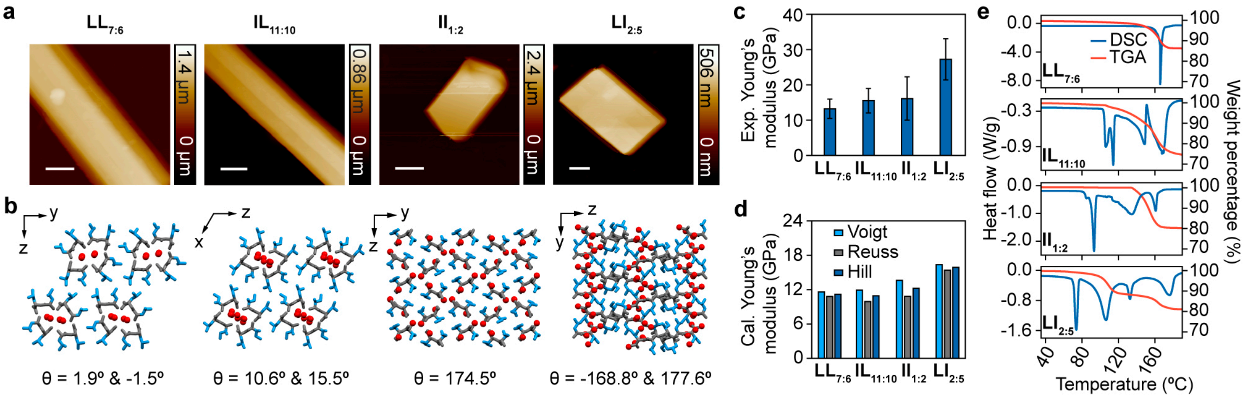

Fig. 3 | Dipeptide crystals. a, AFM topography images of **LL$_{7:6}$** (scale bar, 600 nm), **IL$_{11:10}$** (scale bar, 600 nm), **II$_{1:2}$** (scale bar, 2 µm), and **LI$_{2:5}$** (scale bar, 1 µm). **b**, Crystal structure packing diagrams of **LL$_{7:6}$**, **IL$_{11:10}$**, **II$_{1:2}$**, and **LI$_{2:5}$**. The side chains, backbone, and water molecules are colored in blue, grey, and red. **c**,**d**, Average measured (**c**) and calculated (**d**) Young's moduli of **LL$_{7:6}$**, **IL$_{11:10}$**, **II$_{1:2}$**, and **LI$_{2:5}$** crystals. The calculations incorporate van der Waals dispersion effects using the Voigt-Reuss-Hill approximation and Tkatchenko-Scheffler (TS) scheme. **e**, DSC and TGA profiles of **LL$_{7:6}$**, **IL$_{11:10}$**, **II$_{1:2}$**, and **LI$_{2:5}$** crystals.

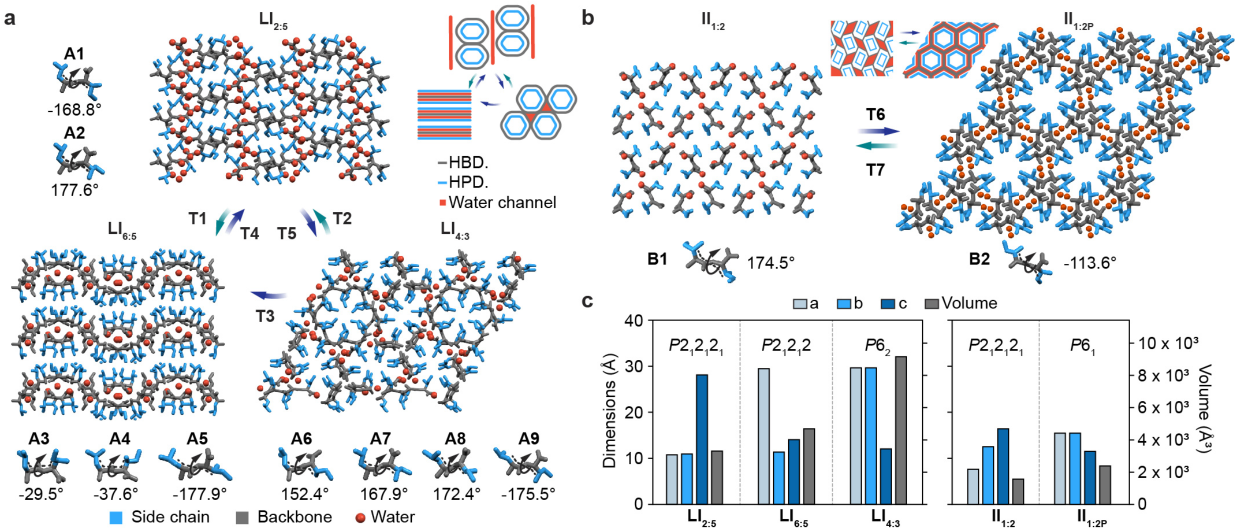

Fig. 4 | Reversible phase transitions of LI and II crystals in response to temperature and RH changes. a, Crystal structures of three interconvertible **LI** hydrates (**T1-T5** represent phase transition conditions with **T1** = 55 °C/50% RH, **T2** = 60 °C/50% RH, **T3** = 70 °C/50% RH, **T4** and **T5** = 25 °C/> 97 % RH). The schematic shows the changes in relative orientations of the hydrophobic domains (colored in blue) and hydrophilic water channels (colored in red). **A1-A9** represents θ values of various conformers of the corresponding structure. **b**, Crystal structures of **II**$_{1:2}$ and **II**$_{1:2P}$ that is interconvertible at conditions **T6** and **T7** (**T6** = 95 °C/40% RH and **T7** = 25 °C/ > 97 % RH). **B1** and **B2** represent θ values of various conformers of the corresponding structure. **c**, Unit cell dimensions and volume of **LI** and **II** crystals.

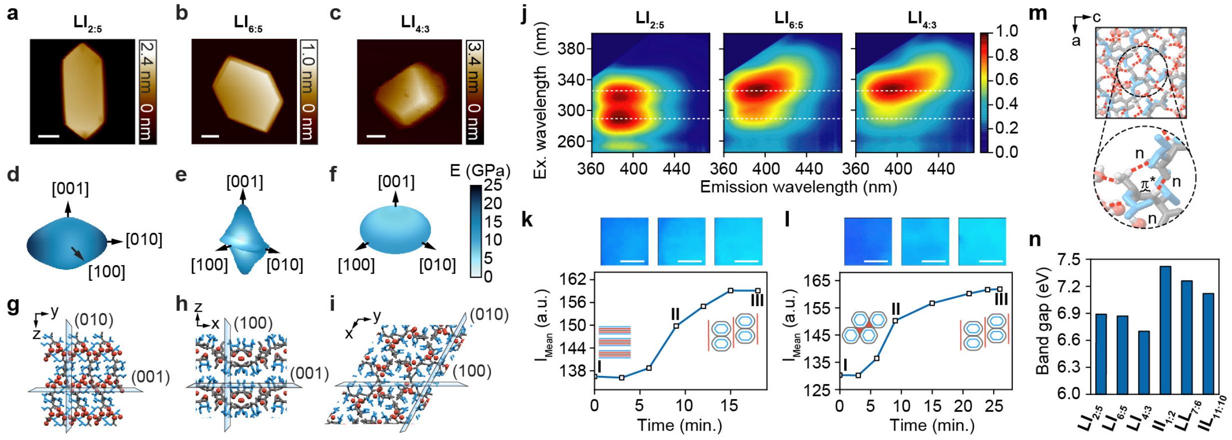

Fig. 5 | Mechanical properties and intrinsic fluorescence of LI crystals. a–c, AFM topography images of **LI$_{2:5}$** (**a**), **LI$_{6:5}$** (**b**), and **LI$_{4:3}$** (**c**). The scale bars are 4 µm for (**a**) and 2 µm for (**b**) and (**c**). **d–f**, 3D distribution of calculated Young's modulus of (**d**) **LI$_{2:5}$**, (**e**) **LI$_{6:5}$**, and (**f**) **LI$_{4:3}$** crystals. **g–i**, Crystal structures showing (001), (010), and (001) planes of (**g**) **LI$_{2:5}$**, (**h**) **LI$_{6:5}$**, and (**i**) **LI$_{4:3}$**. **j**, 3D fluorescence contour maps of **LI$_{2:5}$**, **LI$_{6:5}$**, and **LI$_{4:3}$** crystals recorded at 25 °C and 50% RH. **k**,**l**, Plot of mean intensity (I_{mean}) *vs* time, during the phase transition of **LI$_{6:5}$** to **LI$_{2:5}$** (**k**), and **LI$_{4:3}$** to **LI$_{2:5}$** (**l**), excited at 290 nm. The corresponding photographs at three different time intervals of transformation are shown above the plots. The scale bar represents 5 mm. **m**, Crystal structures of **LI$_{2:5}$** showing the distribution of the HOMO, which exhibits *n* character, and the LUMO which displays π character (π*), along the O atoms and the amide bond, respectively. **n**, Comparison of the band gaps of dipeptide crystals.